

QUARTERLY JOURNAL

OF THE

ROYAL METEOROLOGICAL SOCIETY

Vol. 112

APRIL 1986

No. 472

Quart. J. R. Met. Soc. (1986), **112**, pp. 293–313

551.515.81

A comparison between frontogenesis in the two-dimensional Eady model of baroclinic instability and summertime cold fronts in the Australian region

By MICHAEL J. REEDER and ROGER K. SMITH

Geophysical Fluid Dynamics Laboratory, Monash University, Clayton, Victoria, Australia 3168

(Received 12 March 1985; revised 23 September 1985)

SUMMARY

A two-dimensional, anelastic, numerical model with a simple turbulence parametrization is integrated with Eady's linear normal mode solution for an unstable baroclinic wave as initial condition. The structure of the surface front which develops after five days of model integration is compared with data on summertime cold fronts, or 'cool changes', in south-eastern Australia obtained during recent field experiments of the Australian Cold Fronts Research Programme. It is shown that the ridge–trough structure of an amplifying baroclinic wave and its attendant surface front captures many of the important features of 'cool changes', together with the broad-scale flow in which they develop. Indeed, it is argued that the model provides a useful theoretical framework in which the dynamics of the Australian summertime 'cool change' may be understood.

1. INTRODUCTION

The introduction of frontal analysis on mean sea level synoptic charts by Bjerknes and the Norwegian School of meteorologists around 1920 led to the view that extratropical cyclogenesis was associated with some kind of instability of the newly discovered polar front. However, as more upper air data became available and as the theory of quasi-geostrophic motion advanced, the idea that cyclogenesis is a direct manifestation of frontal instability altered and the existence of fronts came to be recognized as a consequence, rather than a cause, of extratropical cyclogenesis. The change of view was precipitated by the pioneering studies of baroclinic instability by Charney (1947) and Eady (1949). These demonstrated that unstable waves having the structural features and energy conversions of extratropical cyclones, and with corresponding space scales and growth rates, can evolve spontaneously in a broad baroclinic shear flow as opposed to a narrow frontal zone. In contrast, analyses of instability on frontal surfaces by Solberg and Høiland (see Petterssen, 1956, sections 15.5, 15.6, and refs.) cannot account for these features.

Although the precise relationship between classical baroclinic instability theory and cyclogenesis in the atmosphere is obscured by the fact that many extratropical cyclones evolve from pre-existing finite amplitude disturbances and not from incipient ones, it has been shown that growing baroclinic waves develop patterns of horizontal deformation and shear which act on their temperature fields to initiate frontogenesis (or frontolysis), see e.g. Williams (1967), Hoskins and Bretherton (1972), Mudrick (1974), Hoskins (1976), Hoskins and West (1979), Hoskins and Heckley (1981). As a result of these studies, the view has emerged that middle latitude fronts are secondary, but nevertheless important phenomena associated with extratropical cyclogenesis.

Frontogenesis in south-eastern Australia in summer appears at first sight to have no more than a tenuous connection with extratropical cyclogenesis, since cyclones are generally far south of the Australian continent. Indeed, frontogenesis at Australian latitudes at this time of year takes place in the col region between two anticyclones, a situation depicted well by the average summertime (December–February) mean sea level isobars shown in Fig. 1. In general, however, fronts do extend southwards to a parent depression at much higher latitudes, a typical synoptic situation being that shown in Fig. 2. While the depression itself must be studied as a fully three-dimensional problem, the front at lower latitudes may be regarded to a good first approximation as two dimensional. With this observation in mind, we shall show that the theory of frontogenesis in a developing baroclinic wave is not only relevant to the Australian region, but that with surface friction effects included, the simple two-dimensional Eady model captures many of the observed features of summertime cold fronts (known locally as ‘cool changes’) at Australian latitudes and provides a suitable dynamical framework in which to understand them.

The basic Eady problem (Eady 1949) concerns the linear instability of a uniform zonal shear flow in thermal wind balance with a linear meridional temperature gradient and confined between rigid horizontal planes. In its simplest form, the motion is taken to be two dimensional, independent of the meridional direction, and inviscid on an f plane. While Eady’s perturbation solution is valid only for the initial development of a so-called baroclinic wave, it displays a number of quite realistic features in relation to extratropical cyclogenesis; in particular, for a growing wave:

- (i) the warmest air is eastward of the surface trough;
- (ii) the phase lines of pressure and meridional velocity tilt westwards with height;
- (iii) the fastest growing wave is approximately of zonal wavenumber six; and
- (iv) the steering level is in the middle troposphere.

Furthermore, starting with this solution as the initial condition, Williams (1967) integrated an inviscid, two-dimensional, Boussinesq, primitive equation model numerically and demonstrated that a surface cold front forms as the Eady wave grows to finite amplitude. The front forms in the contracting Eady wave trough, sandwiched to the east

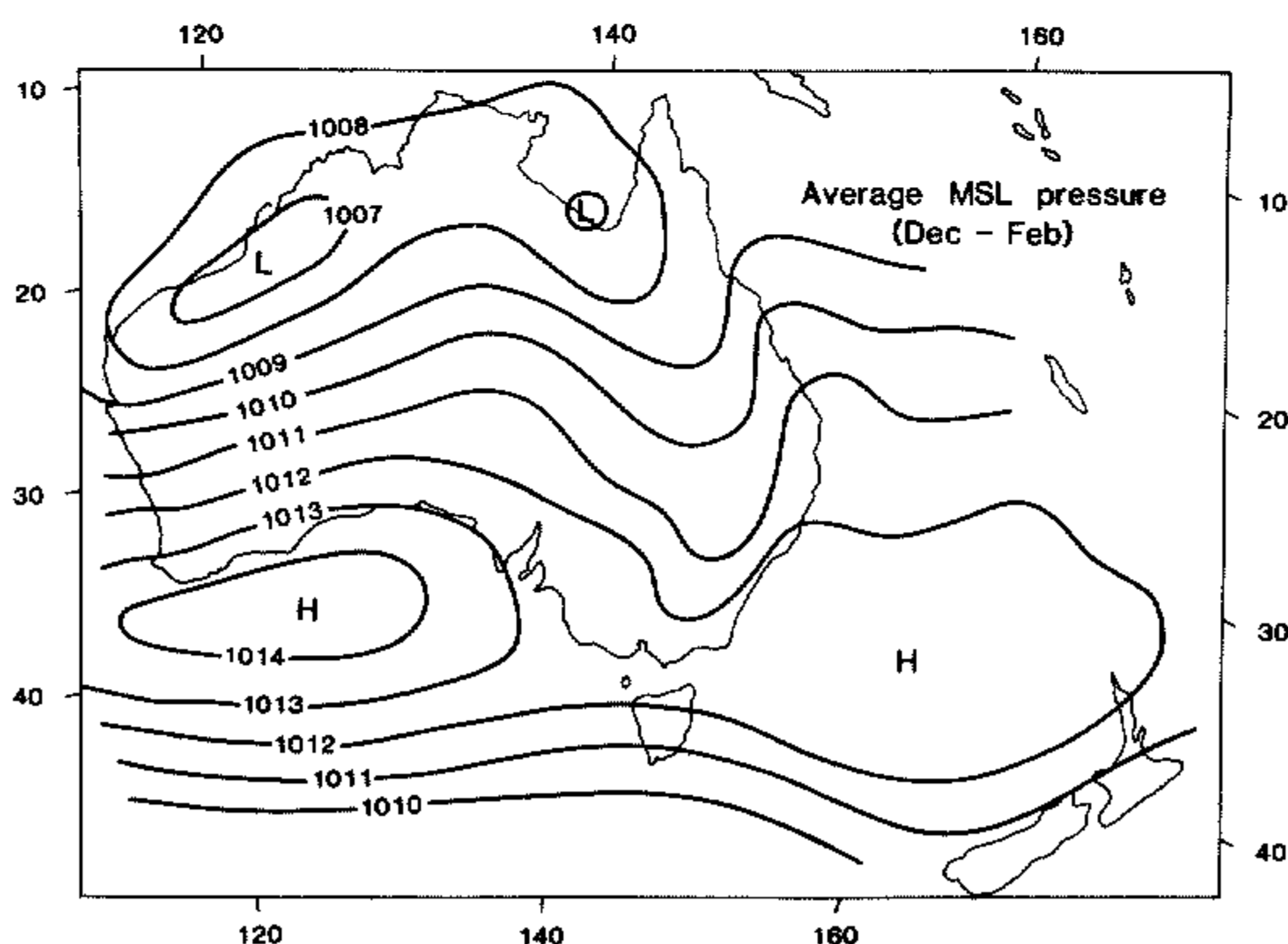


Figure 1. The average summertime (December to February) mean sea level isobars for the Australian region.

and west by broader-scale high pressure regions. In the southern hemisphere model configuration (negative Coriolis parameter) there are warm northerlies ahead of the front, cool southerlies behind and the maximum surface temperature occurs just ahead of the surface front. This structure is clearly a good first approximation to the summertime situation in south-eastern Australia, typified by that shown in Fig. 2.

Since about half of summertime 'cool changes' are 'dry' (Berson and Reid 1957; see also Clarke 1961), it would seem reasonable to ignore precipitation processes and possibly also latent heat release in an initial study, but earlier comparisons of theory with observations (e.g. Blumen 1980; Keyser and Anthes 1982) suggest that frictional processes may not be ignored.

The principal effects of friction on the Eady wave were investigated by Barcilon (1964) who included Ekman boundary layer pumping at horizontal boundaries in the Eady problem. This approach was later employed by Hoskins and Bretherton (1972) and Blumen (1980) in a study of frontogenesis in the semi-geostrophic analogue of the Eady problem. In a detailed comparison of model results with observational data on an intense cold front over the United States reported by Sanders (1955), Blumen concluded that the Ekman suction representation of surface friction is too crude to account for the observed structure of vertical motion in fronts. However, greater realism was achieved by Keyser and Anthes, who integrated numerically a compressible, hydrostatic, primitive equation model which included a high resolution planetary boundary layer parametrization due to Blackadar (1978).

In the present study the structure of the cold front which forms in the two-dimensional Eady configuration is compared in detail with that of summertime cold fronts in the south-eastern Australian region as revealed by data from observational phases I and II of the Australian Cold Fronts Research Programme (ACFRP) (Smith *et al.* 1982). The model calculations are based on integrations of a two-dimensional, anelastic, hydrostatic, numerical model in streamfunction-vorticity form, similar to that used by Orlanski and

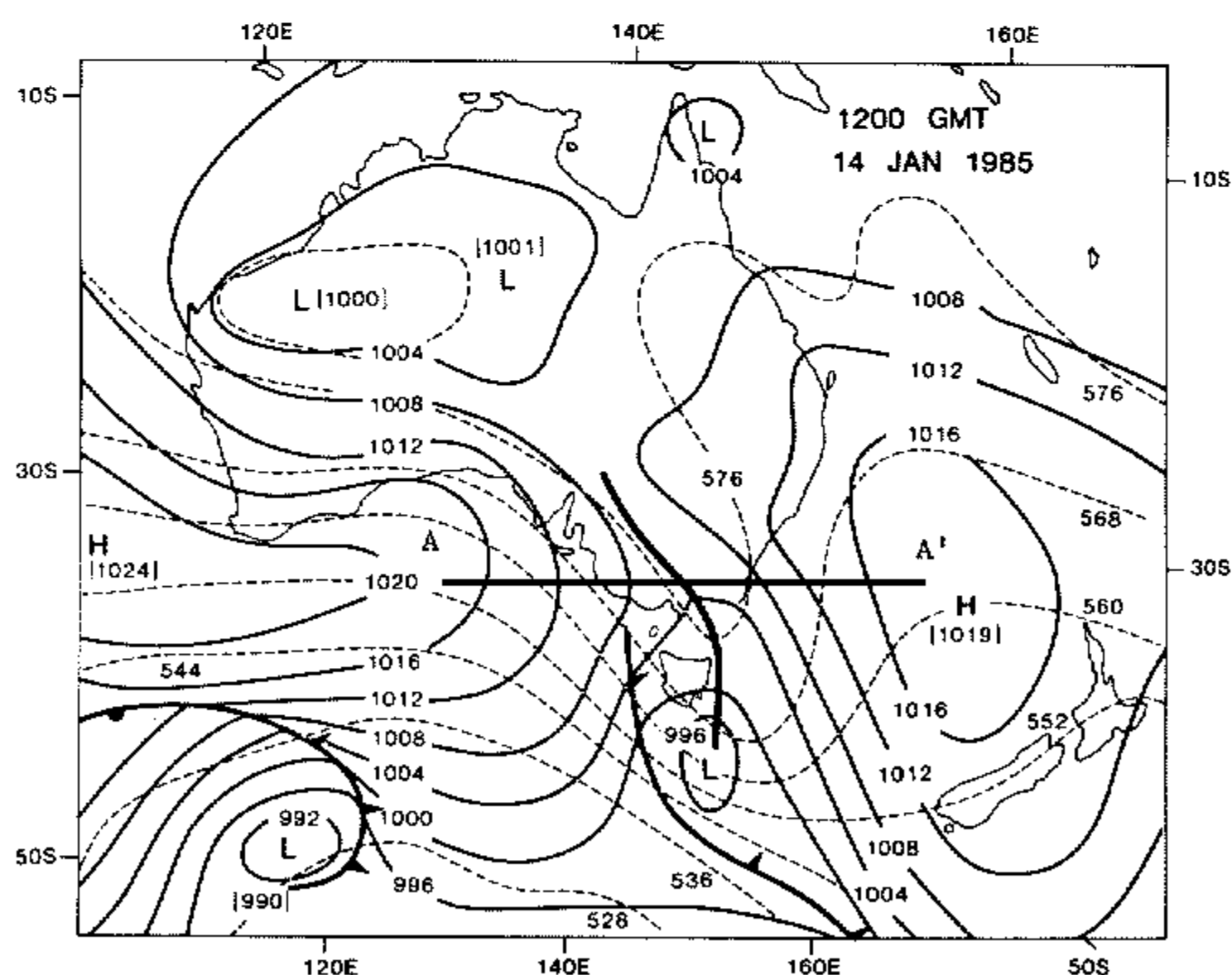


Figure 2. Mean sea level isobaric analysis with 1000–500 mb thickness lines (dashed, in decametres) superimposed for a typical summertime situation in the Australian region. Prominent features are the surface cold front and associated prefrontal trough (thick solid line) over south-eastern Australia, sandwiched between two anticyclones. Hot continental northerly flow precedes the front with cooler maritime south-westerlies behind.

Note that the thermal ridge is approximately co-located with the prefrontal trough.

Ross (1977), starting with Eady's linear normal mode solution as initial condition. The model includes a representation of boundary layer friction intermediate in sophistication between those used by Blumen (1980) and Keyser and Anthes (1982).

2. THE MODEL

Although the model configuration is similar to that used many times previously (e.g. Williams 1967; Hoskins and Bretherton 1972; Blumen 1980; Keyser and Anthes 1982), there are notable differences in detail and in method of solution. Accordingly, a brief description is a necessary preliminary to the presentation of comparisons with observations.

(a) Flow configuration

We investigate the growth of an unstable baroclinic wave in a uniform zonal shear flow bounded by rigid horizontal surfaces and in thermal wind balance with a linear meridional temperature gradient on an f plane. The configuration is shown in Fig. 3. A rectangular coordinate system (x, y, z) is chosen with the x (zonal) coordinate translating with uniform speed $\frac{1}{2}U$, with y pointing northwards and z vertically. In terms of this, the basic zonal flow is defined by $(\bar{u}(z), 0, 0)$ for $0 \leq z \leq H$, where

$$\bar{u}(z) = (U/H)z - \frac{1}{2}U, \quad (1)$$

H being the total depth of flow. The corresponding potential temperature field has the form

$$\Theta(y, z) = \theta_0(z) - (f\theta_{00}U/gH)y, \quad (2)$$

where $\theta_0(z) = \theta_s + \Gamma z$ defines the vertical structure, f is the Coriolis parameter and g is the acceleration due to gravity. The constant quantities in Eqs. (1) and (2) are chosen as follows: $U = 40 \text{ m s}^{-1}$, $H = 10^4 \text{ m}$, $\theta_{00} = 308 \text{ K}$, $\theta_s = 288 \text{ K}$, $\Gamma = 4 \times 10^{-3} \text{ K m}^{-1}$, $g = 9.8 \text{ m s}^{-2}$, $f = -10^{-4} \text{ s}^{-1}$, the negative value of f allowing the conventional coordinate orientation with y northwards to be used in the southern hemisphere context. Com-

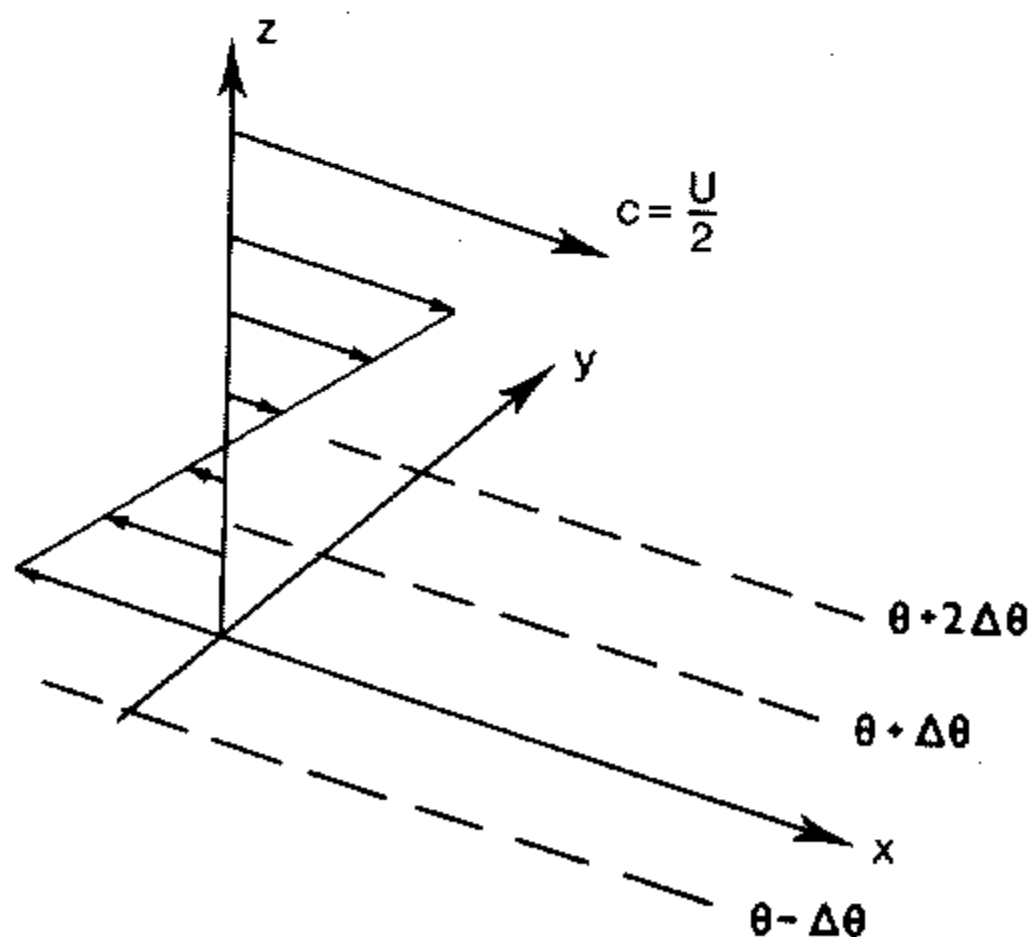


Figure 3. A schematic representation of the coordinate system and initial flow configuration. The x , y , z coordinates point eastwards, northwards and upwards, respectively, and translate to the east with a constant speed $\frac{1}{2}U$.

compressibility effects are allowed for by an anelastic formulation (Ogura and Phillips 1962) with vertical density structure $\rho_0(z)$. The latter is determined in terms of the surface pressure p_s and the function $\theta_0(z)$ through the hydrostatic equation, i.e. $\rho_0(z) = -g^{-1}dp_0/dz$ where

$$p_0(z) = 10^5 \left\{ \left(\frac{p_s}{10^5} \right)^\kappa - \frac{g}{c_p} \int_0^z \frac{dz}{\theta_0(z)} \right\}^{1/\kappa} \text{ in Pa,}$$

where $\kappa = R/c_p$, c_p is the specific heat of dry air and R is the specific gas constant in SI units.

(b) *Formulation of the equations*

The anelastic forms of the momentum, continuity and thermodynamic equations are

$$\partial \mathbf{V} / \partial t + (\mathbf{V} \cdot \nabla) \mathbf{V} + f \mathbf{k} \wedge \mathbf{V} = -\nabla(p/\rho_0) + g(\theta'/\theta_{00})\mathbf{k} + \mathbf{D}_M \quad (3)$$

$$\nabla \cdot (\rho_0 \mathbf{V}) = 0 \quad (4)$$

and

$$\partial \theta / \partial t + \mathbf{V} \cdot \nabla \theta = D_H \quad (5)$$

where $\mathbf{V} = (u, v, w)$ is the velocity vector, p is the perturbation pressure, θ is the potential temperature and θ' its deviation from $\Theta(y, z)$, \mathbf{k} is the unit vector $(0, 0, 1)$ and \mathbf{D}_M and D_H represent the turbulent diffusion of momentum and heat respectively. The latter are defined by

$$\mathbf{D}_M = K_M^x \nabla_h^2 \mathbf{V} + \partial \tau^z / \partial z \quad (6)$$

and

$$D_H = K_H^x \nabla_h^2 \theta' + \frac{\partial}{\partial z} (K_H^z \partial \theta' / \partial z) \quad (7)$$

where τ^z is the vertical component of stress. In the interior of the domain $\tau^z = K_M^z \partial \mathbf{V} / \partial z$, so that the horizontal and vertical diffusion processes are modelled independently with different but constant diffusion coefficients K_M^x , K_M^z , K_H^x , and K_H^z , superscripts denoting the direction and subscripts the diffused quantity. For definiteness, we have assumed a turbulent Prandtl number K_M/K_H of unity and chosen $K^x = 10^4 \times K^z$ in each case.

All dependent variables are assumed to be independent of y , except for the constant meridional potential temperature gradient in Eq. (2). Then Eq. (4) can be satisfied by introducing the streamfunction ψ defined by

$$u = (1/\rho_0) \partial \psi / \partial z, \quad w = -(1/\rho_0) \partial \psi / \partial x.$$

The meridional component of vorticity is defined by $\eta = \partial u / \partial z - \partial w / \partial x$. Two-dimensionality allows Eqs. (3) and (5) to be expressed in terms of η , v and ψ in preference to u , v and w . Then

$$\frac{\partial \eta}{\partial t} - J\left(\psi, \frac{\eta}{\rho_0}\right) = f \frac{\partial}{\partial z} - \frac{g}{\theta_{00}} \frac{\partial \theta'}{\partial x} + K_M^x \frac{\partial^2}{\partial x^2} \eta + \frac{\partial^2}{\partial z^2} (K_M^z \eta) \quad (8)$$

$$\frac{\partial v}{\partial t} - \frac{1}{\rho_0} J(\psi, v) = -\frac{f}{\rho_0} \frac{\partial \psi}{\partial z} + f \bar{u} + K_M^x \frac{\partial^2}{\partial x^2} v + \frac{\partial}{\partial z} \left(K_M^z \frac{\partial v}{\partial z} \right) \quad (9)$$

$$\frac{\partial \theta}{\partial t} - \frac{1}{\rho_0} J(\psi, \theta) = -v \frac{\partial \Theta}{\partial y} + K_H^x \frac{\partial^2}{\partial x^2} \theta + \frac{\partial}{\partial z} \left(K_H^z \frac{\partial \theta}{\partial z} \right) \quad (10)$$

where the Jacobian $J(\alpha, \beta) = (\partial\alpha/\partial x)(\partial\beta/\partial z) - (\partial\alpha/\partial z)(\partial\beta/\partial x)$, and the vorticity satisfies the diagnostic equation,

$$\eta = \frac{1}{\rho_0} \frac{\partial^2 \psi}{\partial x^2} + \frac{\partial}{\partial z} \left(\frac{1}{\rho_0} \frac{\partial \psi}{\partial z} \right). \quad (11a)$$

Typically, for both synoptic and frontal-scale motions, $w \ll u$ and the horizontal length scale $L \gg H$, so that to a good approximation Eq. (11a) may be represented by the hydrostatic form

$$\eta = \frac{\partial}{\partial z} \{ (1/\rho_0) \partial \psi / \partial z \}. \quad (11b)$$

A description of the method of solution of Eqs. (8)–(11) is given in appendix A.

(c) Boundary conditions

At the top and bottom boundaries ($z = H$ and $z = 0$) we impose a free-slip and a no-slip boundary condition respectively. Since we shall be studying disturbances which are zonally periodic (see below), periodic boundary conditions are specified at the lateral boundaries.

In terms of a streamfunction–vorticity formulation, the no-slip requirement $\mathbf{V} = 0$ at $z = 0$ is satisfied by

$$\psi|_{z=0} = v|_{z=0} \equiv 0$$

and

$$\eta|_{z=0} = (2\psi/\rho_0 z^2)|_{z=\delta z} + (U/z)|_{z=\delta z} - \frac{1}{2}U\rho_0(\partial\rho_0^{-1}/\partial z)|_{z=0}. \quad (12)$$

The latter condition gives the surface vorticity in terms of the streamfunction evaluated at height $z = \delta z$, and can be derived by expanding η in a Taylor series about $z = 0$. In addition to boundary conditions on η , v and ψ we require a condition on the vertical component of the stress τ^z . Assuming no-slip and a logarithmic wind profile near the boundary, an expression for the surface stress in terms of the meridional component of velocity and the streamfunction evaluated at height $z = \delta z$ is

$$\tau^z|_{z=0} = \rho_0(u_*^2/U_s)[(1/\rho_0)\partial\psi/\partial z + \frac{1}{2}U, v]_{z=\delta z} \quad (13)$$

where the magnitude of the horizontal wind is

$$U_s = [\{ (1/\rho_0)\partial\psi/\partial z + \frac{1}{2}U \}^2 + v^2]^{1/2}$$

and the friction velocity u_* is defined by

$$u_*^2 = \left[k_* \frac{U_s}{\ln(z/z_0)} \right]_{z=\delta z}^2.$$

$k_* \equiv 0.4$ is von Kármán's constant and $z_0 = 0.5$ m is the roughness length. Strictly, Eq. (13) defines the stress at $z = z_0$, but for the purposes of this study we shall take it to define the stress at $z = 0$. Note that the surface stress is calculated in earth-fixed coordinates; not in the moving reference frame. The surface condition on the potential temperature is that there be no heat flux through the boundary, i.e. $K_H^z \partial \theta' / \partial z \equiv 0$ as in Keyser and Anthes (1982).

At $z = H$ the boundary conditions are

$$K_M^z \partial v / \partial z = K_H^z \partial \theta' / \partial z = K_M^z (\eta - \partial \bar{u} / \partial z) = 0$$

and

$$\psi = \int_0^H \rho_0 \partial \bar{u} dz.$$

The basic flow defined by Eqs. (1) and (2), while satisfying a no-slip condition at $z = 0$, does not satisfy the boundary conditions on the stress. Consequently the flow adjusts to the imposed constraints through the evolution of a boundary layer which reaches a steady state in about twenty-four hours when no perturbation is added.

(d) Initial conditions

At the initial instant ($t = 0$) a small amplitude perturbation is added to the basic state, defined by Eqs. (1) and (2). The perturbation, described in appendix B, is the exact normal mode solution of the linearized, Boussinesq, inviscid, quasi-geostrophic equations found by Eady (1949). Figure 4 shows the form of the perturbation. The wavelength of the perturbation is taken to be 4000 km, which, according to the linear theory, corresponds to the most unstable normal mode.

Although the perturbation is only an approximate solution of Eqs. (8)–(11), since these include viscous terms and a height-varying density, it may be expected to excite the most unstable modes of the system provided its amplitude is sufficiently small. Justification for this procedure is provided by *a posteriori* examination of the solution.

3. RESULTS

We present now the results of a typical integration and compare them with data for summertime cold fronts in south-eastern Australia analysed by Garratt *et al.* (1985). In the calculation described $K_M^z = K_H^z = 15 \text{ m}^2 \text{ s}^{-1}$, while $K_M^x = K_H^x = 1.5 \times 10^5 \text{ m}^2 \text{ s}^{-1}$. The latter value is similar to that used by Williams (1974) and broadly equivalent to that used by Keyser and Anthes (1982) when allowance is made for the fact that the latter authors employ fourth-order horizontal diffusion. Nevertheless, it is appropriate to consider the implications of our choice. In the two-dimensional configuration, the linear poleward decrease of potential temperature represents an unlimited source of available potential energy for a growing baroclinic wave and presumably, therefore, for frontogenesis. However, a simple scale analysis of Eq. (5) suggests that frontogenesis may be counterbalanced by diffusion when K_M^x, K_H^x are of order $5 \times 10^5 \text{ m}^2 \text{ s}^{-1}$. Integrations of our model for a range of horizontal diffusivities have shown that both cyclogenesis and frontogenesis are not sustained for more than a few days for diffusivities higher than about this value, and in such cases, instead of achieving a steady state, the Eady wave decays (see Reeder 1985). For diffusivities smaller than about $5 \times 10^5 \text{ m}^2 \text{ s}^{-1}$, the structure of the wave is relatively insensitive to the magnitude of the horizontal diffusivity, although a larger diffusivity reduces the rate at which frontogenesis occurs. Accordingly, we shall display features of the disturbance structure at two selected times during the model integration when a strong cold front has formed.

Figure 4 shows the x – z cross-section of the isotachs of meridional (along-front) velocity, isolines of perturbation potential temperature, isentropes of potential temperature, perturbation streamlines and isopleths of vertical (relative) vorticity for the initial perturbation. These cross-sections are appropriate to the southern hemisphere configuration in which cyclonic relative vorticity is negative in sign. The principle features of the initial Eady wave perturbation are summarized in section 2(d). The corresponding cross-sections after five days of real time integration, but with isopleths of vertical velocity replacing the perturbation potential temperature isentropes, are shown in Fig. 5.

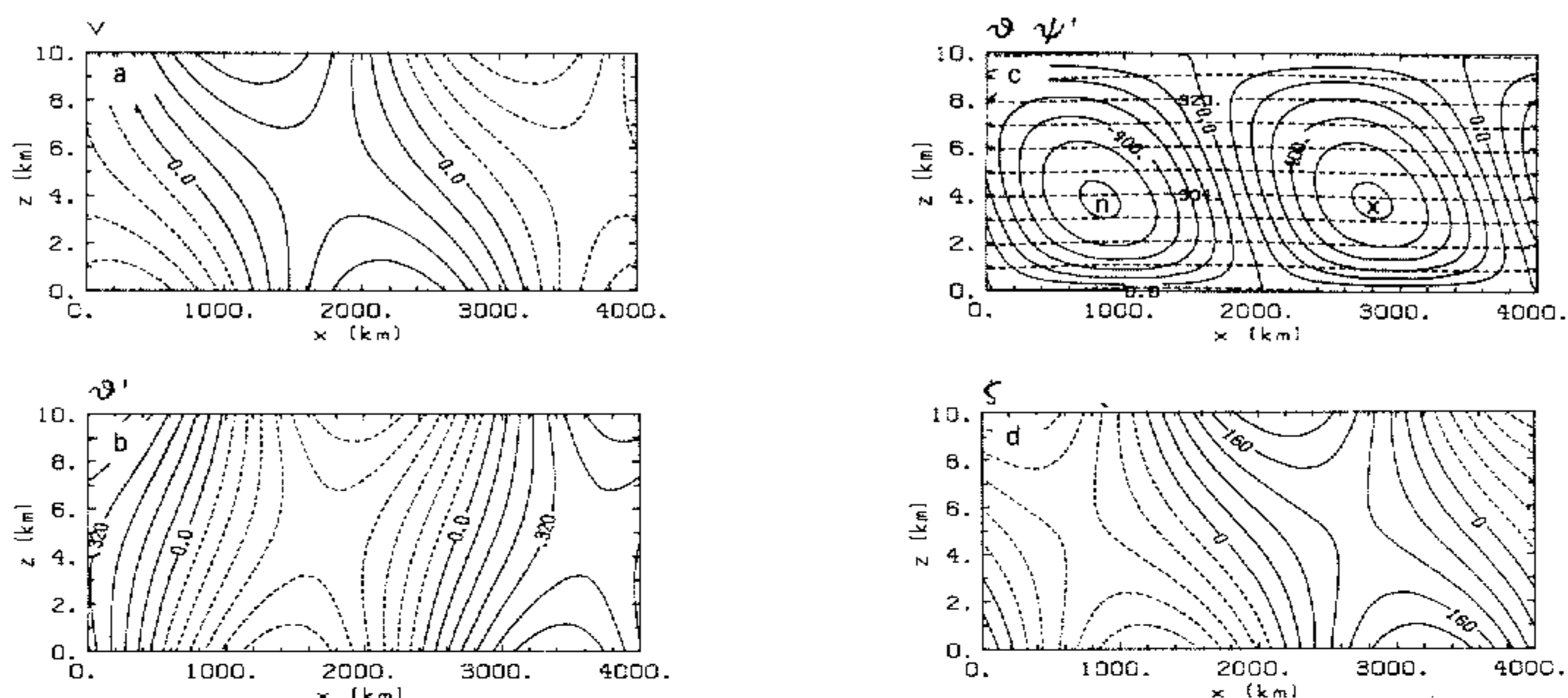


Figure 4. Isopleths of (a) along-front velocity v , (b) perturbation potential temperature θ' , (c) potential temperature θ (dashed lines) and perturbation streamfunction ψ' (solid lines) and (d) relative vorticity ζ at the initial instant, $t = 0$. Contour intervals are 0.3 m s^{-1} , 0.08 K , 3 K , 100 kg m s^{-1} and $4.0 \times 10^{-7} \text{ s}^{-1}$, respectively. Dashed contours denote negative values in (a) and (b) and anticyclonic vorticity ($\zeta > 0$) in (d). The signs of the streamline contours in (c) are indicated by x (positive) and n (negative).

Comparison of Figs. 4 and 5 shows that after five days, an intense front has formed at the upper boundary in the vicinity of $x = 800 \text{ km}$ and that a slightly more diffuse cold front has formed at the surface in the region near $x = 1400 \text{ km}$. The intense upper-level front is, of course, an unrealistic feature produced by modelling the tropopause by a rigid lid and is not of interest here. Accordingly, we focus our attention on the surface cold front and show x - z cross-sections corresponding with Fig. 5 for a longitudinal section of the lowest 3 km of the model and for an integration time of 5.5 days. Throughout the discussion we *define* the position of the surface front to be that of the maximum horizontal

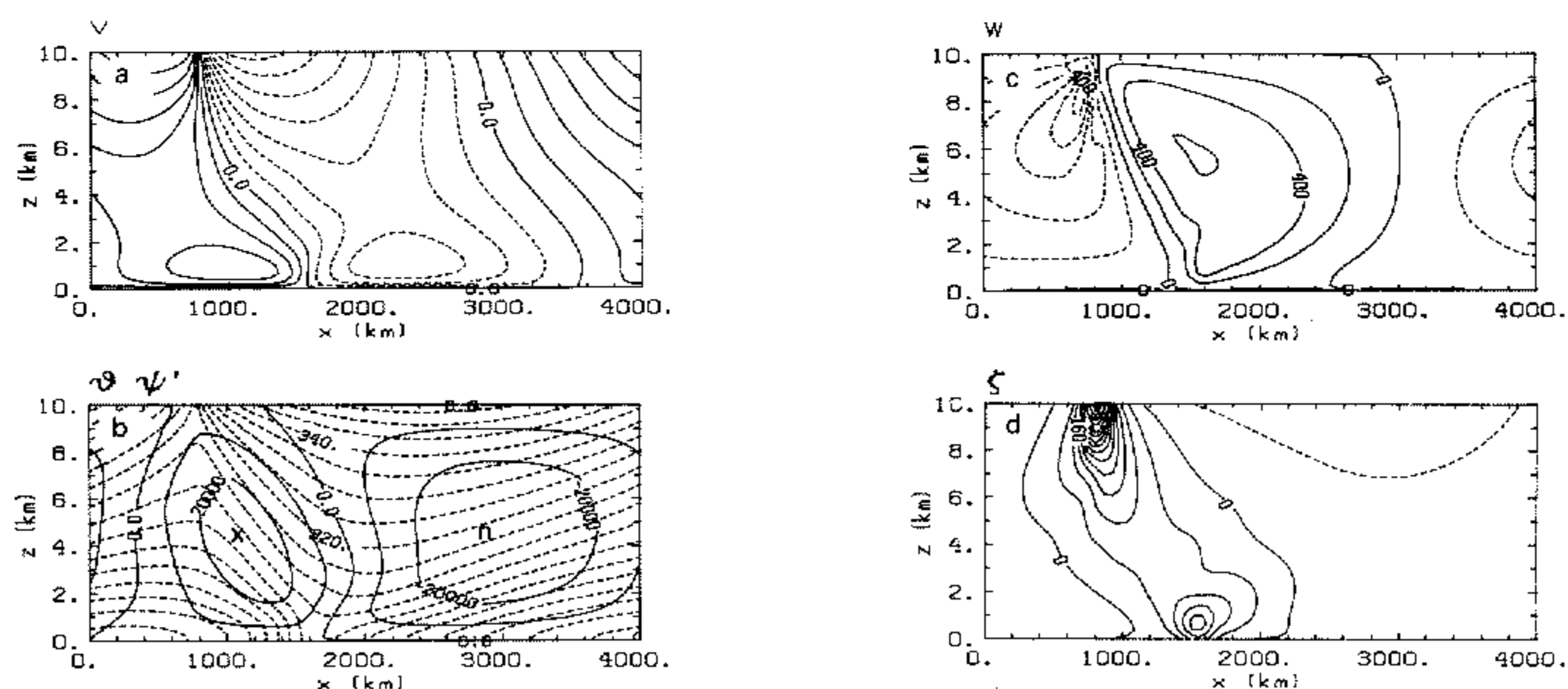


Figure 5. Isopleths of (a) along-front velocity v ; (b) potential temperature θ (dashed lines) and perturbation streamfunction ψ' (solid lines); (c) vertical velocity w ; and (d) relative vorticity ζ after 5 days of model integration. Contour intervals are 6 m s^{-1} , 3 K , $4 \times 10^3 \text{ kg m s}^{-1}$, 2 cm s^{-1} , $4 \times 10^{-5} \text{ s}^{-1}$, respectively. Dashed lines denote negative values in (a) and (c) and anticyclonic vorticity ($\zeta > 0$) in (d). The signs of the streamline contours in (b) are indicated by x (positive) and n (negative).

temperature gradient, located from a cubic interpolation of grid point surface (potential) temperature values. This is contrary to the definition adopted by Blumen (1980), but is preferred here because frontogenesis is discussed in terms of horizontal potential temperature gradient changes.

The isotachs of the along-front velocity component are shown in Fig. 6(a). These are very similar in structure to observed along-front winds in summertime cold fronts in south-eastern Australia, a composite of which is shown in Fig. 6(b). This composite is based on data from events 2, 3 and 4 of the ACFRP phase II experiment, henceforth referred to as the 'fronts experiment'. As is normally the case in the southern hemisphere, the along-front winds have a northerly component ahead of the front and a southerly component behind; prominent features of both the model and the observations are the low-level jets ahead of and behind the cold front, with core maxima at or below a height of 1 km. The depth of the postfrontal jet is shallower than that of the prefrontal jet in both cases, but the strengths of the pre- and postfrontal jets are larger by factors of about one and a half and three, respectively, than those observed, and they are also larger in horizontal extent. Such unrealistically large jet velocities have been noted in previous studies of Eady wave frontogenesis (Williams 1967; Hoskins and Bretherton 1972; Keyser and Anthes 1982), but the reason for them vis-à-vis the model assumptions has not been determined. In several model runs with different frictional coefficients we have been unable to reduce simultaneously the strengths and sizes of the low-level jets. Moreover, Hsie *et al.* (1984) note that with the inclusion of latent heat effects, the prefrontal low-level jet "moves closer to the frontal zone", but that both "upper and lower level jets are stronger". There remains the possibility that the deficiency of the model with regard to the jet strengths and sizes is intrinsic to the assumption of two-dimensionality. Indeed, Hoskins (personal communication) finds that the strong winds in the two-dimensional Eady wave reduce by about 30% in going to the three-dimensional modes studied in Hoskins and West (1979) and in simulations of the life cycle of baroclinic waves by Simmons and Hoskins (1978, 1980). Surface friction is then necessary to reduce the jet speeds to values comparable with observations.

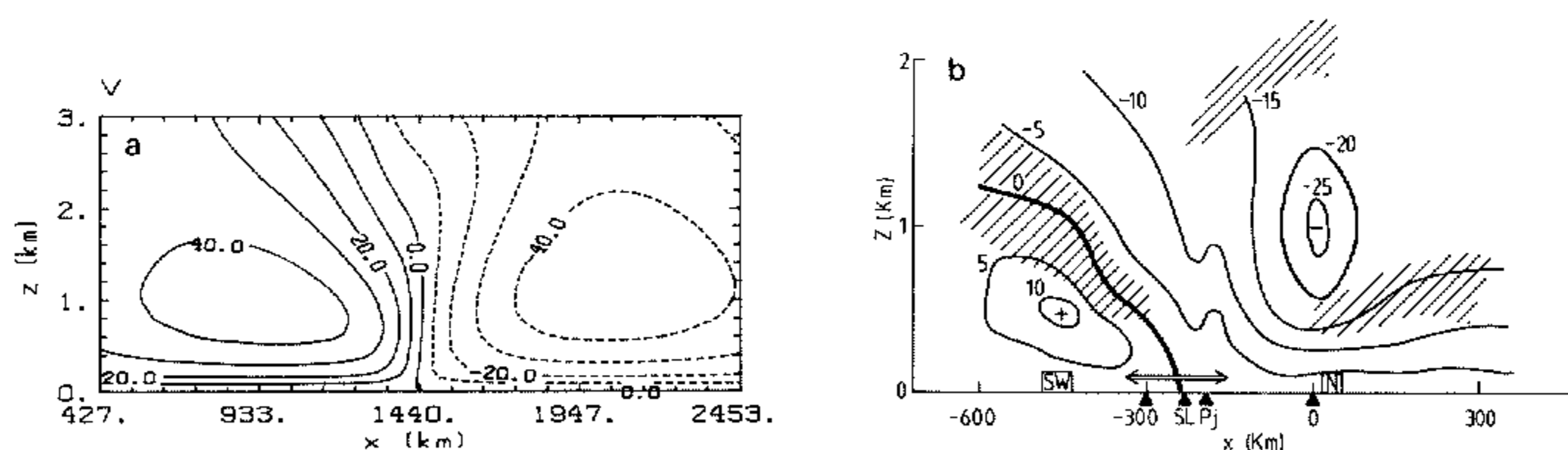


Figure 6. (a) Isotachs of along-front velocity, v , at 5.5 days in a longitudinal section of the lowest 3 km of the model. Contour interval is 5 m s^{-1} . (b) Composite isotachs of v for Australian summertime cold fronts (adapted from Garratt *et al.* 1985).

Figure 7 compares the x - z cross-section of vertical velocity in the model at 5.5 days with data from the fronts experiment. The important features in the model simulation are the region of strong ascent ahead of the front with a vertical velocity maximum of 9 cm s^{-1} at a height of one kilometre, and the region of relatively uniform subsidence (velocities ~ 1 – 3 cm s^{-1}) in the cold air behind the front. This structure is in good agreement with the observed time cross-sections, although at 5.5 days the model tends

to underestimate the prefrontal vertical velocity maximum and slightly to exaggerate the horizontal scale of the vertical jet. In this regard, three points are worth noting. Firstly, our calculations for different diffusivities have shown that the prefrontal vertical velocity maximum is the quantity most affected by a change in the vertical diffusion coefficient, the jet intensity increasing with K_M^z . This is as expected since the prefrontal vertical jet is associated with low-level frictional convergence. Secondly, the inclusion of moist processes tends also to increase the strength of the vertical jet (Hsie *et al.* 1984) and all three observed fronts in Fig. 7 were accompanied by precipitation at the ground. Finally, such a strong vertical jet as in the model is not captured by the Ekman parametrization of friction (Blumen 1980).

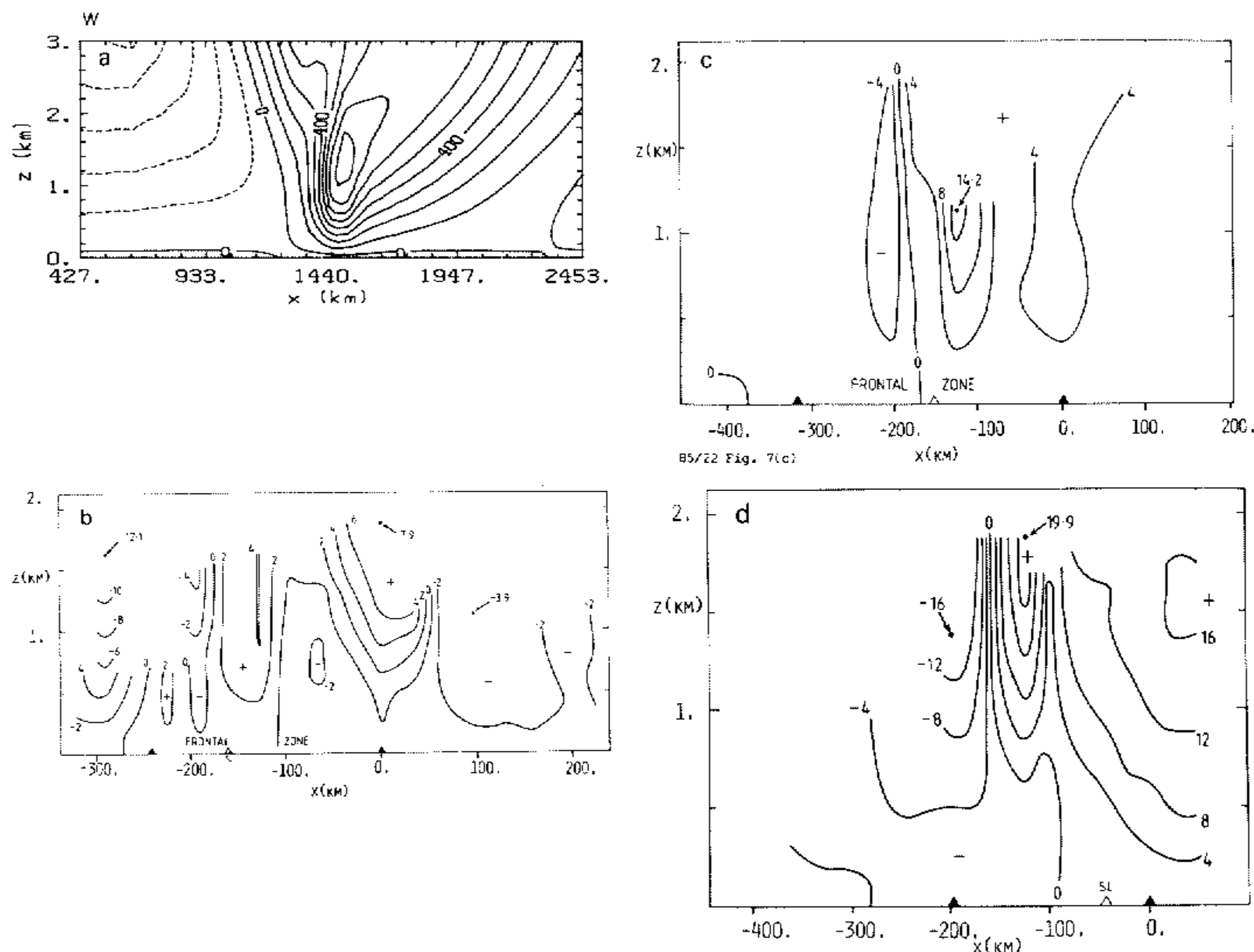


Figure 7. (a) Vertical velocity isotachs in a longitudinal section of the lowest 3 km after 5.5 days of model integration. Contour interval is 1 cm s^{-1} . Dashed lines denote negative values. (b), (c), (d) show corresponding time cross-sections for events 2, 3 and 4 of the Cold Fronts Experiment (adapted from Garratt *et al.* 1985). Contour values are as labelled in cm s^{-1} .

In all three ACFRP field experiments, low-level wind structure was determined in considerable detail during frontal passages. This was accomplished by hourly (and during certain periods half-hourly) pilot balloon soundings, equivalent to a horizontal resolution of order 50 km, comparable with the grid spacing of 53 km in our model. The data for the first two* experiments showed that, except possibly in relatively small regions within the frontal transition zone, there was substantial front-relative flow *through the front* towards the cold air (see e.g. Reeder *et al.* 1982; Garratt *et al.* 1985; see also Clarke 1961). There was no sustained low-level 'feeder flow' towards the front in the cold air as

* At the time of writing, phase III data are in the process of being analysed.

in a steady laboratory gravity current (Simpson 1982) and in no sense could the front be regarded as a material boundary as is often supposed to be the case (e.g. Wallace and Hobbs 1977, pp. 114–117). It is, therefore, of particular interest to compare the calculated relative flow normal to the front with that observed. First, however, it is appropriate to consider the motion of the front itself.

Figure 8 shows the positions of the maximum surface potential temperature gradient and maximum cyclonic relative vorticity as functions of time. In the chosen reference frame which moves with the mid-level zonal flow ($\frac{1}{2}U$), the front moves westward with an average speed of 2.3 m s^{-1} , while at 5.5 days its speed is only 1.7 m s^{-1} . These speeds correspond respectively with eastward translations of 17.7 m s^{-1} and 18.3 m s^{-1} relative to the ground. The relative vorticity maximum lies initially some 700 km to the east of the surface temperature gradient maximum, but moves eastwards more slowly relative to the ground so that at 5.5 days, the separation is only about 200 km. It may be noted that the westward regression of both the front and the relative vorticity maximum in the moving frame is a consequence of the decrease in density with height (Green 1960; Keyser and Anthes 1982) and the presence of friction; for the inviscid, Boussinesq, Eady wave the position of the surface vorticity maximum remains unchanged, while the front moves eastwards towards it (see the dashed curves in Fig. 8). In the Boussinesq version of the present model, the westward regression of the front, also shown in Fig. 8, is less rapid than in the anelastic version and is in accord with Blumen's calculations (Blumen 1980).

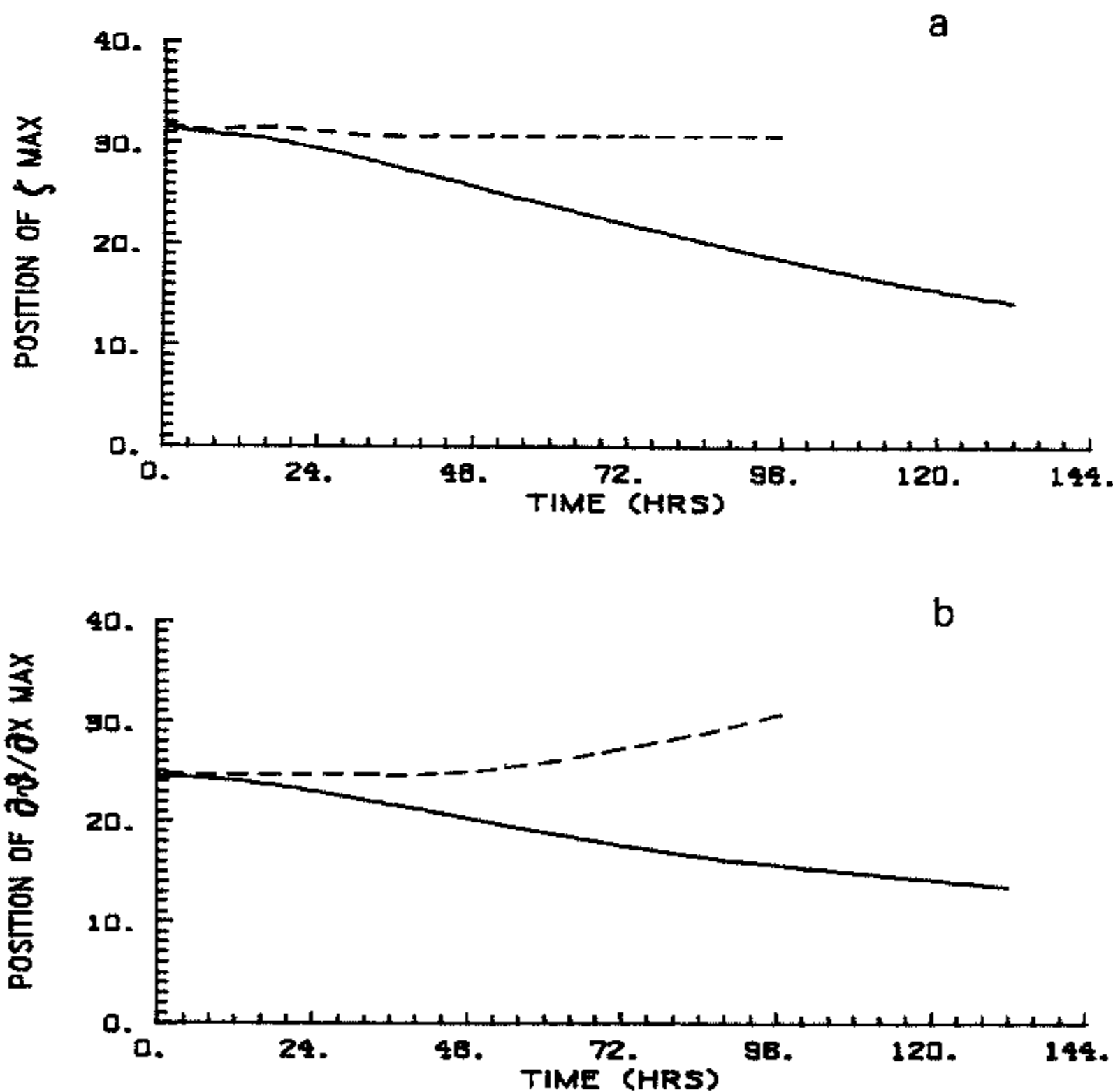


Figure 8. The horizontal position in 10^2 km of (a) the maximum cyclonic vorticity ζ_{max} at the surface and (b) the maximum surface temperature gradient as functions of model integration time. The dashed lines in each case are for the inviscid, Boussinesq model for which the integration was terminated at 96 hours.

The isotachs of $u - c$, the airflow relative to the front, where c is the speed of the front, are shown in Fig. 9(a) for the lower atmosphere at 5.5 days. At this time the flow is almost everywhere westward relative to the front, except for a small region in the lowest 600 m just behind the front where there is eastward relative flow. It is significant that this small region of advected flow develops at a late stage in the simulation; at five days, for example, the relative flow is still everywhere westward. The results appear to be consistent with Blumen's calculations. In a study of parcel trajectories, Blumen (1980, Fig. 8) showed that for the inviscid, Boussinesq problem, particle motions are westward relative to the front except at a late stage (about 5 days) in the region below the frontal inversion where there develops a weak motion towards the front. In contrast, Blumen (p. 75) noted that, when Ekman friction is included, the particle trajectories are everywhere westward relative to the mid-level steering current. However, Blumen does not show the front relative motion and since the inclusion of Ekman friction effectively lowers the steering level for the baroclinic wave (see Williams and Robinson 1974, Fig. 5; and compare Blumen's Figs. 3 and 8), the front moves westward relative to the mid-level flow, in contrast to the inviscid case when it (as defined herein) moves eastwards. When the motion of the front is taken into account, it is probable that our results and Blumen's agree.

Figure 9(b), taken from Garratt *et al.* (1985), shows a composite time-height cross-section for u , measured in a stationary reference frame during the fronts experiment. The region between D_1 and D_f delineates the frontal transition zone in which there may occur several 'lines of change' at the surface; these are generally associated with the passage of squall lines (SL). The so-called final line (D_f) marks the place at which the surface pressure begins its steady rise and is the feature which shows most continuity as the front evolves. This line is normally analysed as the surface front position and its passage heralds the onset of steady surface cooling. Typically, this line moves eastwards at $10\text{--}15\text{ ms}^{-1}$. It follows that there is significant westerly flow relative to the surface front, except possibly in a small region within the frontal transition zone. The same is true of individual events and is entirely consistent with model calculations. Neither the observations nor the model accord with the more traditional view of a front as a translating material boundary between two air-masses. However, a note of caution is necessary concerning the identification of the small region of advected flow in the model with that observed. In the latter case, the region of eastward relative flow is approximately co-located with a prefrontal squall line, itself moving eastward relative to the front, and which may produce a gust front at the surface (Garratt *et al.* 1985). The latter has the

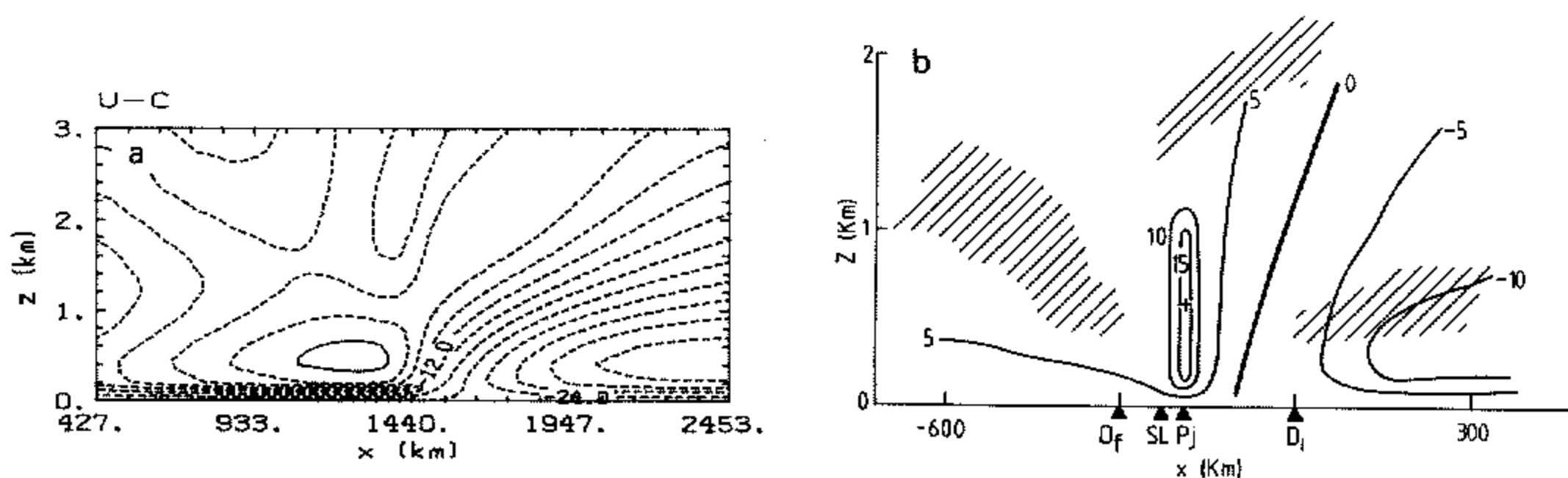


Figure 9. (a) Isotachs of relative cross-front velocity, $u - c$, in a longitudinal section of the lowest 3 km after 5.5 days of model integration, c being the speed of the front. Contour interval is 3 ms^{-1} . Note the small region of positive relative flow just behind the surface front. (b) Composite isotachs of u for Australian summertime cold fronts (adapted from Garratt *et al.* 1985). Typical observed speeds of fronts are of the order of 15 ms^{-1} , so that the relative flow is almost everywhere negative, as in the model.

local structure of a gravity current with a region of positive advected flow ($u - c > 0$) relative to its head, and hence relative to the line D_f . Hence, a balloon sounding through the squall line outflow will suggest advected flow which may be typical of the meso- β -scale squall line circulation rather than the larger-scale frontal circulation. Indeed, in the model, the advected flow region occurs predominantly in the cold air behind the surface front (Fig. 9(a)) whereas it is generally observed within the frontal transition region. This raises some important questions concerning the relationship between fronts and gravity currents and the circumstances under which fronts develop gravity-current-type features. These questions are beyond the scope of the present study.

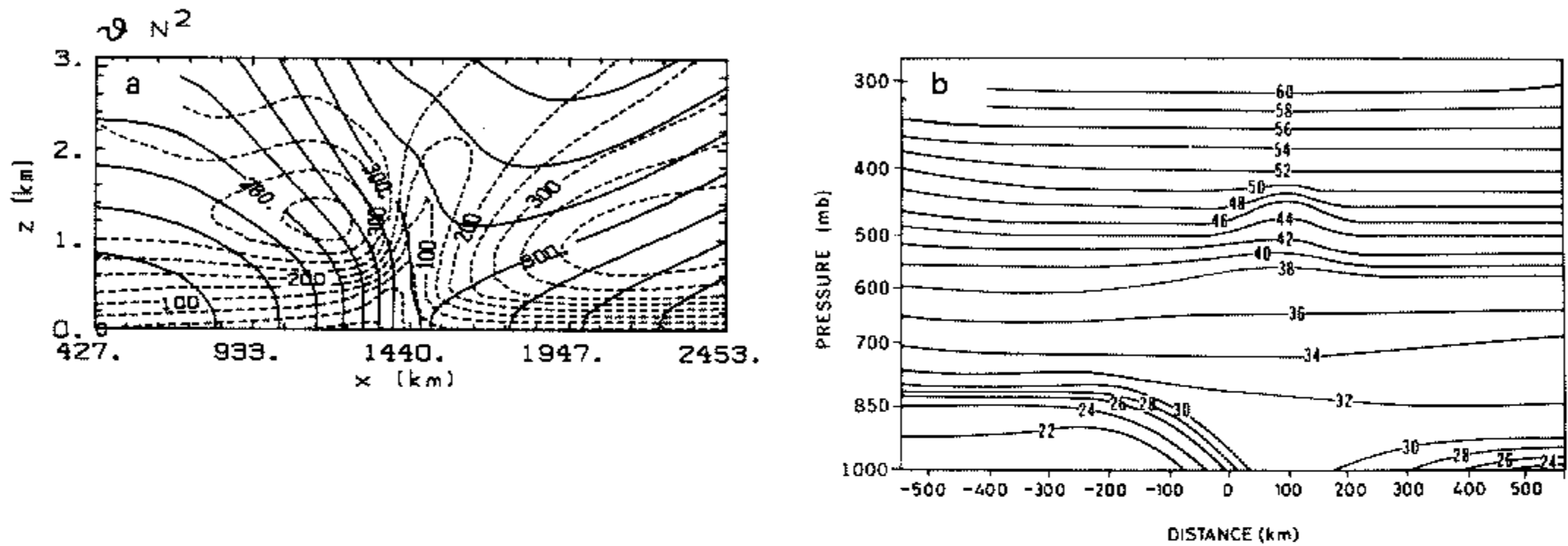


Figure 10. (a) Isentropes (solid lines) and isopleths of N^2 (dashed lines) from the model at 5.5 days. Contour intervals are 3 K and $5 \times 10^{-5} \text{ s}^{-2}$, respectively. (b) Composite of isentropes for summertime 'cool changes', reproduced from Ryan and Wilson (1985).

Figure 10 shows the x - z cross-section of potential temperature and Brunt-Väisälä frequency together with a composite time cross-section of potential temperature from the fronts experiment. In the model, neutral or slightly unstable lapse rates develop in the cold air behind the front since the postfrontal jet maximum and hence the cold air advection maximum is located about 1 km above the surface. In the postfrontal region there is a very stable layer above the cold air. This may be attributed partly to the effect of subsidence and partly to the conversion of horizontal potential temperature gradient to vertical gradient by differential advection by the vertically sheared ageostrophic cross-front velocity component, the latter being the dominant effect (Keyser and Anthes 1982, p. 1798). Comparison of Figs. 10(a) and (b) indicates that in both the model and the observations the cold air is quite shallow, being mostly confined below 3 km (see also Blumen 1980, Figs. 1 and 12). Garratt *et al.* (1985) reported a shallow, convective, postfrontal mixed layer about 0.5–1.0 km deep which would coincide with the region including neutral or slightly unstable lapse rates in the model. The shaded areas in Figs. 5(b) and 9(b) display the most stable regions as determined by Garratt *et al.*; comparison between these and those in the model (Fig. 10(a)) shows close agreement.

At this point it is worth noting the relatively large global increase in static stability ($\sim 66\%$) during five days of a typical integration (cf. Figs. 4(c) and 5(c)). The increase in static stability is a result of the consumption of available potential energy by the growing wave. The relatively large increase is presumably a consequence of the two-dimensional assumption, which implies an unlimited amount of available potential energy and hence an unlimited potential for increasing the static stability. This must be regarded as an unrealistic feature of the two-dimensional Eady model. The increase in static stability may also affect the growth rate of the baroclinic wave itself, as it implies an

increase in the Rossby radius of deformation $L_R = NH/f$. Since the zonal wave number of the wave is fixed by the size of the domain, the product $L_R k$ increases with L_R and, at least on the basis of linear theory, the wave is detuned (recall that linear inviscid Boussinesq theory predicts instability only for $0 < L_R k < 2.4$, with maximum growth rate $0.3U/L_R$ when $L_R k = 1.6$).

The x - z cross-section of relative vertical vorticity in the model is compared with data from three observed cases in Fig. 11. In the model, the main concentration of cyclonic vorticity is in a region about 250 km wide and less than 2 km deep immediately ahead of the surface front (Fig. 11(a)). The maximum vorticity is about $3f$, compared with observed maxima of between $1.5f$ and $2f$. The observed cross-sections show considerable variability amongst themselves and none could be regarded as showing close resemblance to the model in all respects; event 3 (Fig. 11(c)) shows, for example, a concentration of vorticity in the forward part of the frontal zone and below 1.5 km, but in this event, strong ridging occurred before the passage of the final line and this corresponds with the region of anticyclonic vorticity at the rear of the frontal zone. In event 4, there are two local vorticity maxima, but the main region of cyclonic vorticity is mostly ahead of the surface front (identified with the final line). In event 2, the vorticity maximum is close to the surface front and slopes sharply back towards the cold air above 600 m, a feature not evident in the model.

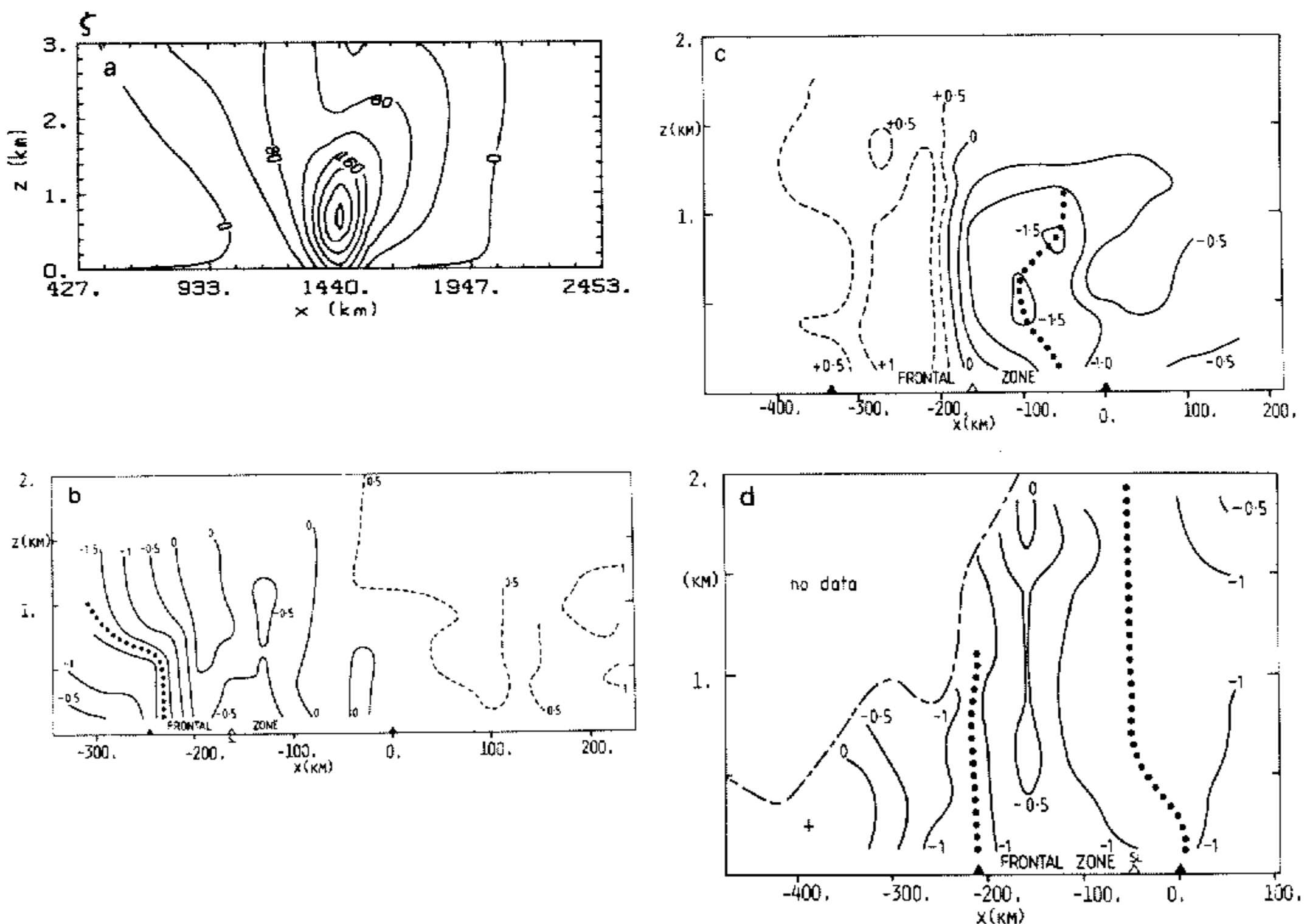


Figure 11. (a) Relative vorticity isopleths in a longitudinal section of the lowest 3 km after 5.5 days of model integration. Contour interval is $4 \times 10^{-5} \text{ s}^{-1}$. Dashed lines denote anticyclonic vorticity ($\zeta > 0$). (b), (c), (d) show corresponding time cross-sections for events 2, 3 and 4 of the Cold Fronts Experiment (adapted from Garratt *et al.* 1985). Contour values are as labelled in units of $0.5 \times 10^{-4} \text{ s}^{-1}$.

The zonal variation of perturbation pressure at a height of 200 m in the model at 5.5 days is shown in Fig. 12. This shows good agreement with the variation of surface pressure

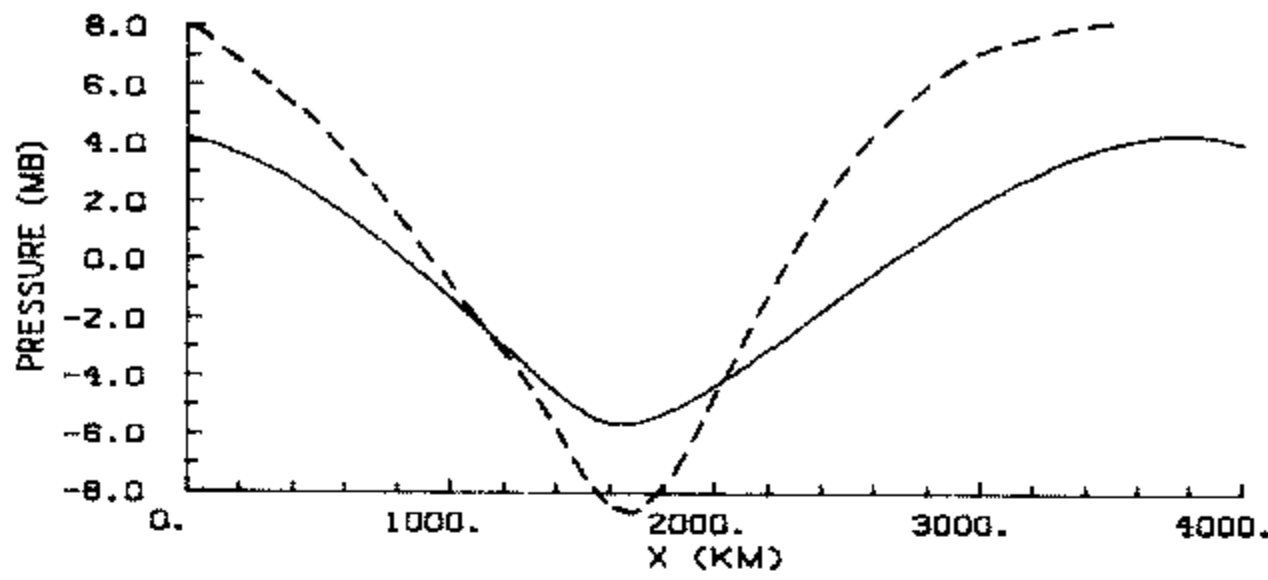


Figure 12. The zonal variation of perturbation pressure at a height of 200 m after 5.5 days of model integration (solid line), and the surface perturbation pressure along the line AA' in Fig. 2 (dashed line).

along the line AA' in Fig. 2. Attention is drawn to the occurrence in the model of a broad trough, some 200 km wide, ahead of the surface front; this corresponds with the frontal transition zone identified in the observations (Garratt *et al.* 1985) and analysed as a prefrontal trough by synopticians (Fig. 2).

The final comparisons concern the rate of frontogenesis represented by the material rate of change of horizontal temperature gradient

$$G = \frac{D}{Dt} |\nabla_h \theta|. \quad (14)$$

Following Miller (1948), an expression for this relevant to the model is

$$G = T_1 + T_2 + T_3 + T_4 \quad (15)$$

where

$$T_1 = \mathbf{n} \cdot \nabla_h D_H \quad T_2 = -\theta_z \mathbf{n} \cdot \nabla_h \mathbf{w} \quad T_3 = -\frac{1}{2} D |\nabla_h \theta|$$

$$T_4 = -\frac{1}{2} (E \theta_x^2 + 2F \theta_x \theta_y - E \theta_y^2) / |\nabla_h \theta|.$$

D is the horizontal divergence $u_x + v_y$; $E = u_x - v_y$ and $F = v_x + u_y$ are the shearing and stretching deformations; and \mathbf{n} is the unit vector in the direction of $\nabla_h \theta$. In this study, $\partial u / \partial y$ and $\partial v / \partial y$ are both identically zero and $\partial \theta / \partial y$ is a constant. In such circumstances, some authors have chosen slightly different diagnostics to (14) such as $D\theta_x / Dt$ (e.g. Sanders 1955; Blumen 1980; Keyser and Anthes 1982) or $D(\frac{1}{2}\theta_x^2) / Dt$ (Thorpe and Nash 1984). The above form is identical to that used by Garratt *et al.* and is the counterpart of the pressure coordinate version used by Ogura and Portis (1982).

The terms T_1 to T_4 represent respectively the rate of frontogenesis due to the horizontal gradient of thermal diffusion in the direction of the existing potential temperature gradient; the rate due to the tilting of vertical into horizontal gradients by differential vertical motion; the rate due to horizontal convergence and that due to horizontal deformation.

Garratt *et al.* calculated the contribution to G from the sum of horizontal convergence and deformation ($T_3 + T_4$) from data obtained during the fronts experiment. Isopleths of this contribution in time–height cross-section are shown in Fig. 13 together with the x – z cross-section from the model at 5.5 days. There is good qualitative agreement between theory and observation in the structure of these fields, the principal feature being the large positive contribution below about 1 km in height and confined mainly within the frontal transition zone, ahead of the surface front. The maximum of $T_3 + T_4$ calculated at 5.5 days is $8.6 \times 10^{-9} \text{ K m}^{-1} \text{ s}^{-1}$. This compares well with the observed values which tend to maximize at $5 \times 10^{-9} \text{ K m}^{-1} \text{ s}^{-1}$, or $4 \text{ K}(100 \text{ km})^{-1}(3 \text{ h})^{-1}$.

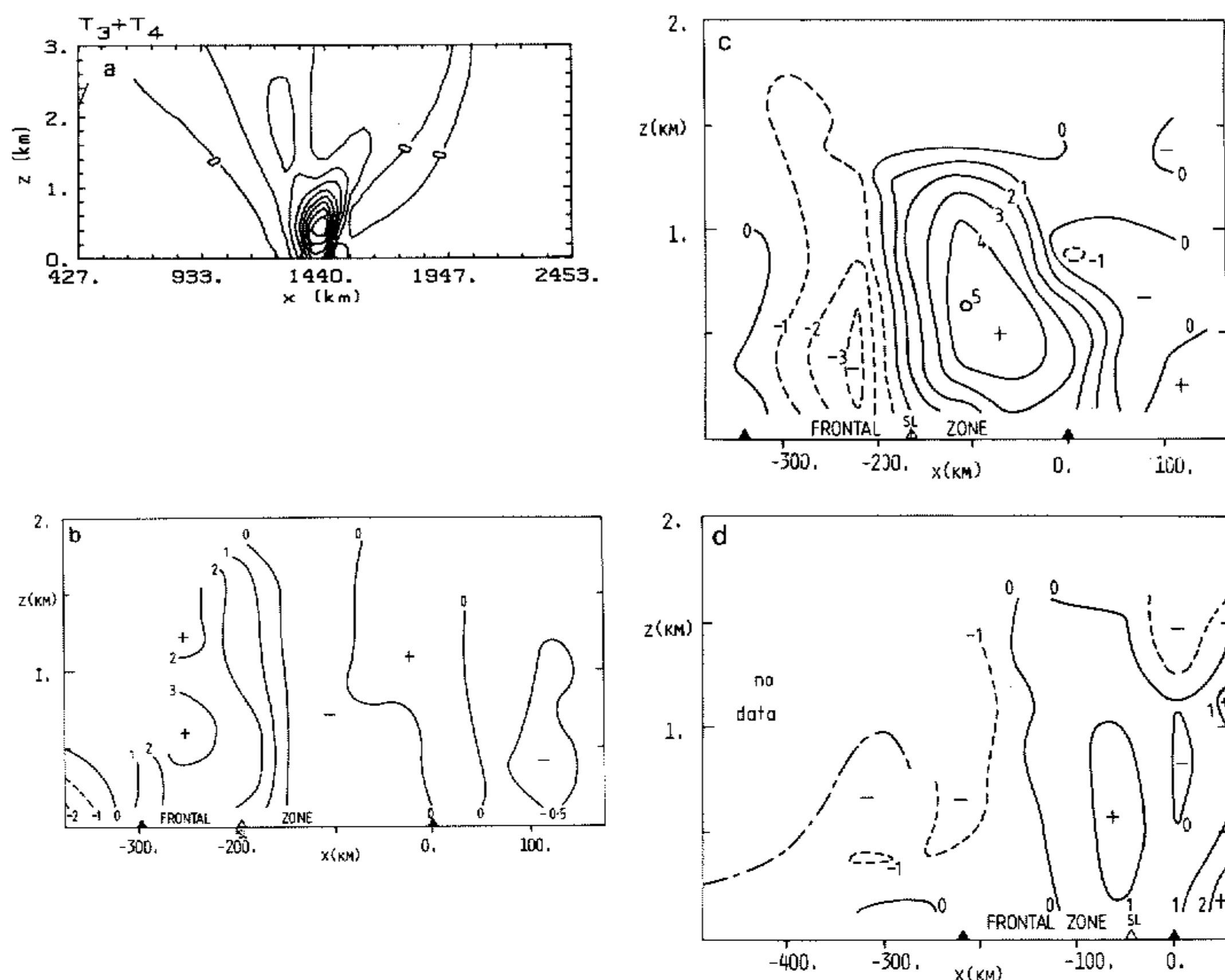


Figure 13. Isopleths of $T_3 + T_4$ in a horizontal section of the lowest 3 km after 5.5 days of model integration. Contour interval $10^{-9} \text{K m}^{-1} \text{s}^{-1}$. Dashed lines denote negative values. (b), (c), (d) show corresponding time cross-sections for events 2, 3, and 4 of the Cold Fronts Experiment (adapted from Garratt *et al.* 1985). Contour values are also $10^{-9} \text{K m}^{-1} \text{s}^{-1}$.

In the model, T_4 gives the major contribution to ΣT_i with a maximum of $6 \times 10^{-9} \text{K m}^{-1} \text{s}^{-1}$, compared with T_3 with a maximum of $3 \times 10^{-9} \text{K m}^{-1} \text{s}^{-1}$, the structure of the two fields being broadly similar to each other, and therefore to the sum $T_3 + T_4$. In contrast, the maximum contribution from T_2 is less than $1 \times 10^{-9} \text{K m}^{-1} \text{s}^{-1}$. This is in sharp contrast to observations (Ogura and Portis 1982; Garratt *et al.* 1985) where T_2 was found to make the largest contribution to ΣT_i . However, observed fields of T_2 are much 'noisier' than those of T_3 and T_4 and may contain significant errors, since fields of vertical motion are themselves difficult to extract from data, let alone their spatial derivatives on which T_2 depends. Generally, diffusion (through T_1) makes an important *frontolytic* contribution in the frontal region with a maximum (in magnitude) of $5 \times 10^{-9} \text{K m}^{-1} \text{s}^{-1}$ and has a lesser *frontogenetic* effect (maximum = $3 \times 10^{-9} \text{K m}^{-1} \text{s}^{-1}$) in small regions above the surface front, apparently due to the anisotropic nature of diffusion in the model. Cross-sections of the individual fields of T_1 to T_4 are given in Reeder (1985).

One disadvantage of the frontogenesis function G is that it relates to tendencies following individual air parcels and conveys maximum information only when the parcel trajectories are known. Recently, Thorpe and Nash (1984) suggested that a more useful diagnostic might be to compute the rate of change of $|\nabla_h \theta|$ in a frame of reference moving with the front i.e.

$$G_c = \frac{D_c}{Dt} |\nabla_h \theta| = \left(\frac{\partial}{\partial t} + c \frac{\partial}{\partial x} \right) |\nabla_h \theta|,$$

c being the speed of the front. Clearly, G and G_c are related by

$$G = G_c + (\mathbf{V} - c\mathbf{i}) \cdot \nabla |\nabla_h \theta| = G_c - T_5, \text{ say,}$$

so that the expression for G_c equivalent to Eq. (15) includes the additional term T_5 on the right-hand side. Cross-sections of T_5 and G_c , which have not been published previously for the Eady problem, are shown in Fig. 14. As might be expected, T_5 gives a negative contribution immediately above the surface front due to vertical advection of the large horizontal temperature gradient (Fig. 14(a)); there is also a smaller positive contribution on each side of the surface front (at 5.5 days) due principally to horizontal advection of the temperature gradient towards the front. The cross-section for G_c (Fig. 14(b)) shows a small region of large positive values *just ahead* of the surface front and below 1 km.

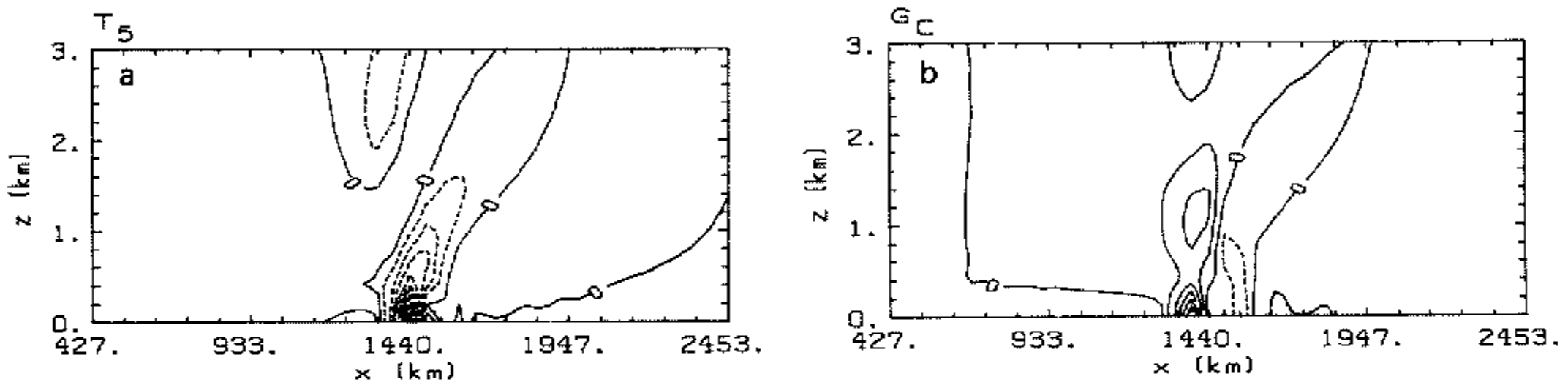


Figure 14. Isopleths of (a) T_5 and (b) G_c in a longitudinal section of the lowest 3 km after 5.5 days of model integration. Dashed contours denote negative values. Contour interval is $10^{-9} \text{K m}^{-1} \text{s}^{-1}$.

This location in relation to the surface front reflects the slight eastward acceleration of the front relative to the ground. The maximum value of G_c , approximately $4 \times 10^{-9} \text{K m}^{-1} \text{s}^{-1}$, is about half the maximum contribution from $T_3 + T_4$, largely on account of the frontolytic effects of T_1 and T_5 . The other prominent feature is the weaker frontolytic region immediately to the east of the main frontogenetic region with a maximum rate of $-2 \times 10^{-9} \text{K m}^{-1} \text{s}^{-1}$. Since observed x - z cross-sections are generally based on time-to-space conversion from serial soundings at fixed locations, implying $(\partial/\partial t)(\text{any quantity}) = -c(\partial/\partial x)(\text{that quantity})$, data-based cross-sections for G_c are not available for comparison.

4. CONCLUSIONS

Eady's linear normal mode solution for an unstable two-dimensional perturbation in a uniform zonal shear flow has been extended into the nonlinear regime using a numerical model. The model is anelastic, includes a simple turbulence parametrization, and is solved by the streamfunction-vorticity method. A detailed comparison is made between a typical model solution and recent data obtained on summertime cold fronts as part of the Australian Cold Fronts Research Programme. It is shown that the ridge-trough structure of an amplifying perturbation and its attendant surface front captures many of the basic features of summertime cold fronts in the Australian region and the broad-scale flow in which they develop. The comparison suggests that the model contains the basic dynamical processes that operate in the region in summertime during surface

frontogenesis. Accordingly, the model would appear to provide a useful dynamical framework in which to obtain a deeper understanding of the Australian summertime 'cool change'.

ACKNOWLEDGMENTS

We thank our colleagues John Garratt, Bill Physick and Brian Ryan from the CSIRO Division of Atmospheric Research, and Ken Wilson from the Australian Bureau of Meteorology for providing data. We wish also to record our appreciation to both Dan Keyser of the NASA Goddard Laboratory for Atmospheres and Paul Mason of the Meteorological Office with whom we have had several stimulating discussions about this work.

APPENDIX A

The numerical scheme

A solution to the coupled set of partial differential equations (8)–(11) is obtained by replacing the continuous forms by an approximating set of finite difference equations defined at regularly spaced discrete points in space and time. The resulting set of algebraic equations for the dependent variables at each discrete point in space and time can be solved in terms of the dependent variables at each discrete spatial point at previous times. In this way the governing partial differential equations are integrated forward in time in a step-wise fashion.

The domain of integration is a rectangular grid in the x – z plane, defined at times $n\Delta t$ ($n = 0, 1, 2, \dots$), with $M + 1$ points in the x direction and $N + 1$ points in the z direction. In this study $\Delta t = 600$ s, $M = 75$ and $N = 50$. The length of the domain, L , is 4000 km and the height of the domain, H , is 10 km, so that the grid dimensions are $\Delta x = L/M = 53.3$ km and $\Delta z = H/N = 200$ m.

Using the notation of Lilly (1964), the differencing operator $\delta_r \phi$ and the averaging operator $\overline{\phi}^r$ are defined as

$$\delta_r \phi = \{\phi(r + \frac{1}{2}\Delta r) - \phi(r - \frac{1}{2}\Delta r)\}/\Delta r$$

$$\overline{\phi}^r = \{\phi(r + \frac{1}{2}\Delta r) + \phi(r - \frac{1}{2}\Delta r)\}/2,$$

where $\phi = \phi(r)$ and Δr is the discrete grid interval in the r direction. In terms of these operators the finite difference analogues of Eqs. (8)–(10) and (11b) are

$$\partial \eta / \partial t = J_1(\psi, \eta / \rho_0) + f \delta_z \bar{v}^2 - (g / \theta_{00}) \delta_x \bar{\theta}^x + K_M^x \delta_{xx} \eta + K_M^z \delta_{zz} \eta \quad (\text{A1})$$

$$\partial v / \partial t = (1 / \rho_0) J(\psi, v) - f \{(1 / \rho_0) \delta_z \bar{\psi}^z - \bar{u}\} + K_M^x \delta_{xx} v + K_M^z \delta_{zz} v \quad (\text{A2})$$

$$\partial \theta / \partial t = (1 / \rho_0) J_2(\psi, \theta) + (f \theta_{00} v / g) \delta_z \bar{u}^z + K_H^x \delta_{xx} \theta + K_H^z \delta_{zz} \theta \quad (\text{A3})$$

$$\eta = \overline{\delta_z \{(1 / \rho_0) \delta_z \bar{\psi}^z\}}^z \quad (\text{A4})$$

where

$$J_1(\alpha, \beta) = \frac{1}{3} \{ 2J_2(\alpha, \beta) + \overline{\delta_x(\alpha \delta_z \bar{\beta}^z)}^x, -\delta_z(\alpha \delta_x \bar{\beta}^x) \}$$

and

$$J_2(\alpha, \beta) = \delta_z(\bar{\beta}^z \delta_x \bar{\alpha}^{xz}) - \delta_x(\bar{\beta}^x \delta_z \bar{\alpha}^{xz}).$$

The Jacobian operators J_1 and J_2 are used for the advection terms in Eqs. (8)–(10) to control the nonlinear instability due to the aliasing of short and long wavelengths. (Arakawa 1966).

The finite difference equations are advanced forward in time using the explicit method of Miller and Pearce (1974). Their procedure involves the alternate use of an Euler scheme and a Matsuno scheme. In summary the method is as follows:
at odd time steps one calculates

$$\phi^*(t + \Delta t) = \phi(t) + \Delta t \frac{\partial \phi}{\partial t}(t),$$

followed by

$$\phi(t + \Delta t) = \phi(t) + \Delta t \frac{\partial \phi^*}{\partial t}(t),$$

while at even time steps one calculates

$$\phi(t + 2\Delta t) = \phi(t + \Delta t) + \Delta t \frac{\partial \phi}{\partial t}(t + \Delta t).$$

The method has an advantage over the more common 'leapfrog' central differencing scheme as it does not produce a split mode and consequently does not require artificial smoothing of the fields.

The numerical procedure consists of solving the prognostic equations (A1)–(A3), at a particular time step, subject to appropriate boundary conditions. The diagnostic equation (A4) is then easily solved for the streamfunction using the well-known method for inverting tri-diagonal matrices.

APPENDIX B

The initial conditions

The perturbation solution corresponding with an inviscid Boussinesq Eady wave follows readily from the quasi-geostrophic potential vorticity equation; in terms of the perturbation variables η' , v' , θ' and ψ' , the solution takes the form

$$\begin{aligned} \eta' = \frac{AUf}{HN^2} k \left\{ \frac{4s^2}{H^2} [PQ(P \sin kx \cosh Z - Q \cos kx \sinh Z + Q \sinh Z) + \right. \\ \left. + Z(P \cos kx \cosh Z + Q \sin kx \sinh Z - P \cosh Z) - \right. \\ \left. - (P \cos kx \sinh Z + Q \sin kx \cosh Z - P \sinh Z)] - \right. \\ \left. - k[PQ(-P \sin kx \cosh Z + Q \cos kx \sinh Z) - \right. \\ \left. - Z(P \cos kx \cosh Z + Q \sin kx \sinh Z) + \right. \\ \left. + (P \cos kx \sinh Z + Q \sin kx \cosh Z)] \right\} \end{aligned} \quad (B1)$$

$$v' = Ak(-P \sin kx \sinh Z + Q \cos kx \cosh Z) \quad (B2)$$

$$\theta' = (Ak.2s/H)(P \cos kx \cosh Z + Q \sin kx \sinh Z) \quad (B3)$$

$$\begin{aligned} \psi' = \left(\frac{AUf}{HN^2} \right) \{ PQ(P \sin kx \cosh Z - Q \cos kx \sinh Z) + \\ + Z(P \cos kx \cosh Z + Q \sin kx \sinh Z) - (P \cos kx \sinh Z + Q \sin kx \cosh Z) \} \end{aligned} \quad (B4)$$

where $P = (1 - s \tanh s)^{1/2}$, $Q = (s \coth s - 1)^{1/2}$, $Z = (2s/H)(z - \frac{1}{2}H)$, $4s^2 = (NH/f)^2 k^2$, $N^2 = (g/\theta_{00})d\theta_0/dz$. A is an arbitrary constant and k is the wavenumber.

The most unstable mode occurs when $s = 0.8$ and consequently $2\pi/k = 4000$ km.

REFERENCES

- | | | |
|---|------|---|
| Arakawa, A. | 1966 | Computational design for long-term numerical integrations of atmospheric motion: Two-dimensional incompressible flow. Part I. <i>J. Computational Phys.</i> , 1 , 119–143 |
| Barcilon, V. | 1964 | The role of Ekman layers in the stability of the symmetric regime obtained in a rotating annulus. <i>J. Atmos. Sci.</i> , 21 , 291–299 |
| Berson, F. A., Reid, D. G. and Troup, A. J. | 1957 | 'The summer cool change of southeastern Australia. I: General behaviour'. Division of Meteorological Physics Tech. Pap. No. 8, CSIRO, Melbourne |
| Blackadar, A. K. | 1978 | 'High resolution models of the planetary boundary layer', in <i>Advances in Environmental Science and Engineering</i> , Vol. 1, J. R. Pfallin and E. N. Ziegler, Eds., Gordon and Breach, 50–85 |
| Blumen, W. | 1980 | A comparison between the Hoskins–Bretherton model of frontogenesis and the analysis of an intense surface frontal zone. <i>J. Atmos. Sci.</i> , 37 , 64–77 |
| Charney, J. G. | 1947 | The dynamics of long waves in a baroclinic westerly current. <i>J. Meteor.</i> , 4 , 135–162 |
| Clarke, R. H. | 1961 | Mesostructure of dry cold fronts over featureless terrain. <i>ibid.</i> , 18 , 715–735 |
| Eady, E. T. | 1949 | Long waves and cyclone waves. <i>Tellus</i> , 1 , 33–52 |
| Garratt, J. R., Physick, W. L., Smith, R. K. and Troup, A. J. | 1985 | The Australian summertime cool change. II: Mesoscale processes. <i>Mon. Wea. Rev.</i> , 113 , 202–223 |
| Green, J. S. A. | 1960 | A problem in baroclinic stability. <i>Quart. J. R. Met. Soc.</i> , 86 , 237–251 |
| Hoskins, B. J. | 1976 | Baroclinic waves and frontogenesis. Part I: Introduction and Eady waves. <i>ibid.</i> , 102 , 103–122 |
| Hoskins, B. J. and Bretherton, F. P. | 1972 | Atmospheric frontogenesis models: Mathematical formulation and solution. <i>J. Atmos. Sci.</i> , 29 , 11–37 |
| Hoskins, B. J. and West, N. V. | 1979 | Baroclinic waves and frontogenesis. Part II: Uniform potential vorticity jet flows—cold and warm fronts. <i>ibid.</i> , 36 , 1663–1680 |
| Hoskins, B. J. and Heckley, W. A. | 1981 | Cold and warm fronts in baroclinic waves. <i>Quart. J. R. Met. Soc.</i> , 107 , 79–90 |
| Hsie, E. Y., Anthes, R. A. and Keyser, D. | 1984 | Numerical simulation of frontogenesis in a moist atmosphere. <i>J. Atmos. Sci.</i> , 41 , 2581–2594 |
| Keyser, D. and Anthes, R. A. | 1982 | The influence of planetary boundary layer physics on frontal structure in the Hoskins–Bretherton horizontal shear model. <i>ibid.</i> , 39 , 1783–1802 |
| Lilly, D. K. | 1964 | Numerical solutions for the shape-preserving two-dimensional thermal convection element. <i>ibid.</i> , 21 , 83–98 |
| Miller, J. E. | 1948 | On the concept of frontogenesis. <i>J. Meteor.</i> , 5 , 169–171 |
| Miller, M. J. and Pearce, R. P. | 1974 | A three-dimensional primitive equation model of cumulonimbus convection. <i>Quart. J. R. Met. Soc.</i> , 100 , 133–154 |
| Mudrick, S. E. | 1974 | A numerical model of frontogenesis. <i>J. Atmos. Sci.</i> , 31 , 869–892 |
| Ogura, Y. and Phillips, N. A. | 1962 | A scale analysis of deep and shallow convection in the atmosphere. <i>ibid.</i> , 19 , 173–179 |
| Ogura, Y. and Portis, D. | 1982 | Structure of the cold front observed in SESAME-AVE III and its comparison with the Hoskins–Bretherton frontogenesis model. <i>ibid.</i> , 39 , 2773–2792 |
| Orlanski, I. and Ross, B. B. | 1977 | The circulation associated with a cold front. Part I: dry case. <i>ibid.</i> , 34 , 1619–1633 |
| Petterssen, S. | 1956 | <i>Weather Analysis and Forecasting</i> . Volume 1. Second Ed., McGraw-Hill |
| Reeder, M. J. | 1985 | 'Models of frontogenesis', Ph.D thesis, Monash University |

- | | | |
|---|------|--|
| Reeder, M. J., Roff, G.,
Smith, R. K., Garratt, J. R. and
Reid, D. G. | 1982 | 'Low level winds'. Bureau of Meteorology. Tech. Rep. No. 51 |
| Ryan, B. F. and Wilson, K. J. | 1985 | The Australian summertime cool change. III: Subsynoptic mesoscale model. <i>Mon. Wea. Rev.</i> , 113 , 224–240 |
| Sanders, F. | 1955 | An investigation of the structure and dynamics of an intense frontal zone. <i>J. Meteor.</i> , 12 , 542–552 |
| Simmons, A. J. and Hoskins, B. J. | 1978 | The life cycle of some nonlinear baroclinic waves. <i>J. Atmos. Sci.</i> , 35 , 414–432 |
| | 1980 | Barotropic influences on the growth and decay of nonlinear baroclinic waves. <i>ibid.</i> , 37 , 1679–1684 |
| Simpson, J. E. | 1982 | Gravity currents in the laboratory, atmosphere and ocean. <i>Ann. Rev. Fluid. Mech.</i> , 14 , 213–234 |
| Smith, R. K., Ryan, B. F.,
Troup, A. J. and Wilson, K. J. | 1982 | Cold fronts research: The Australian summertime "cool change". <i>Bull. Amer. Met. Soc.</i> , 63 , 1028–1034 |
| Thorpe, A. J. and Nash, C. A. | 1984 | Convective and boundary layer parametrizations in a diagnostic model of atmospheric fronts. <i>Quart. J. R. Met. Soc.</i> , 110 , 443–466 |
| Wallace, J. M. and Hobbs, P. V. | 1977 | <i>Atmospheric Sciences: An Introductory Survey</i> . Academic Press |
| Williams, G. P. and Robinson, J. B. | 1974 | Generalized Eady waves with Ekman pumping. <i>J. Atmos. Sci.</i> , 31 , 1768–1776 |
| Williams, R. T. | 1967 | Atmospheric frontogenesis: A numerical experiment. <i>ibid.</i> , 24 , 627–641 |
| | 1974 | Numerical simulation of steady-state fronts. <i>ibid.</i> , 31 , 1285–1296 |